Capella (alpha Aurigae) Revisited : New Binary Orbit, Physical Properties, and Evolutionary State

Torres, G.; Claret, A.; Pavlovski, Krešimir; Dotter, A.

The Astrophysical Journal, 807:26 (15pp), 2015 July 1 doi:10.1088/0004-637X/807/1/26

CAPELLA (α AURIGAE) REVISITED: NEW BINARY ORBIT, PHYSICAL PROPERTIES, AND EVOLUTIONARY STATE

Guillermo Torres[1], Antonio Claret[2], Krešimir Pavlovski[3], and Aaron Dotter[4]
[1] Harvard-Smithsonian Center for Astrophysics, 60 Garden St., Cambridge, MA 02138, USA; gtorres@cfa.harvard.edu
[2] Instituto de Astrofísica de Andalucía, CSIC, Apartado 3004, E-18080 Granada, Spain; claret@iaa.es
[3] Department of Physics, Faculty of Science, University of Zagreb, Bijenička cesta 32, 10000 Zagreb, Croatia; pavlovski@phy.hr
[4] Research School of Astronomy and Astrophysics, Australian National University, Canberra, ACT, 2611, Australia; aaron.dotter@gmail.com
Received 2015 April 29; accepted 2015 May 26; published 2015 June 25

ABSTRACT

Knowledge of the chemical composition and absolute masses of Capella are key to understanding the evolutionary state of this benchmark binary system comprising two giant stars. Previous efforts, including our own 2009 study, have largely failed to reach an acceptable agreement between the observations and current stellar evolution models, preventing us from assessing the status of the primary. Here we report a revision of the physical properties of the components incorporating recently published high-precision radial velocity measurements, and a new detailed chemical analysis providing abundances for more than 20 elements in both stars. We obtain highly precise ($\sim$0.3%) masses of $2.5687 \pm 0.0074\,M_{\odot}$ and $2.4828 \pm 0.0067\,M_{\odot}$, radii of $11.98 \pm 0.57\,R_{\odot}$ and $8.83 \pm 0.33\,R_{\odot}$, effective temperatures of 4970 ± 50 and 5730 ± 60 K, and independently measured luminosities based on the orbital parallax ($78.7 \pm 4.2\,L_{\odot}$ and $72.7 \pm 3.6\,L_{\odot}$). We find an excellent match to stellar evolution models at the measured composition of [Fe/H] $= -0.04 \pm 0.06$. Three different sets of models place the primary star firmly at the end of the core helium-burning phase (clump), while the secondary is known to be evolving rapidly across the Hertzprung gap. The measured lithium abundance, the C/N ratio, and the $^{12}C/^{13}C$ isotopic carbon abundance ratio, which change rapidly in the giant phase, are broadly in agreement with expectations from models. Predictions from tidal theory for the spin rates, spin–orbit alignment, and other properties do not fare as well, requiring a 40-fold increase in the efficiency of the dissipation mechanisms in order to match the observations.

Key words: binaries: general – binaries: spectroscopic – stars: abundances – stars: evolution – stars: fundamental parameters – stars: individual (Capella)

1. INTRODUCTION

As one of the brightest binary stars in the sky, Capella (α Aurigae, HD 34029, HR 1708, HIP 24608, G8 III+G0 III, $P_{\rm orb} = 104$ days, $V = 0.07$) has been studied for more than a century with a wide range of techniques and at all observable wavelengths.[5] A persistent source of frustration for several decades has been the difficulty in determining accurate absolute masses for the components, despite the wealth of astrometric and spectroscopic measurements available. The history of this problem has been related by several authors (e.g., Batten et al. 1975; Barlow et al. 1993), and most recently in our earlier paper (Torres et al. 2009, hereafter T09). The challenge associated with the masses has hindered efforts to pin down the precise evolutionary state of the more massive primary star, which has widely been considered to be a core helium-burning object, based mostly on timescale arguments. Disappointingly, current stellar evolution models have so far largely failed to confirm that notion, as it has not been possible to achieve a satisfactory fit to the global properties of both stars simultaneously at a single age when assuming the bulk chemical composition the system is believed to have. The secondary, on the other hand, is clearly on its way across the Hertzprung gap.

The uncertainty in the masses was thought to have been solved in the T09 analysis, which improved the formal precision by about a factor of three compared to previous estimates, and documented efforts to control systematic errors in the radial velocities that have likely plagued the determination of the velocity amplitude of the rapidly rotating secondary star for decades, as described there. Despite this, it was still not possible to establish the state of the primary component unambiguously when enforcing a single age.

In the interim, Weber & Strassmeier (2011) have presented a new spectroscopic study of Capella based on much higher-quality observational material that leads to significantly larger masses for both stars than in our 2009 study, by several times the stated uncertainties. In particular, the spread in mass between the stars increased from 1% to about 3.5%, which is an enormous difference for a pair of giants, and could drastically change the assessment of their relative state of evolution. In addition, we have now made a new determination of the chemical composition of Capella that is appreciably different from the abundance assumed in the earlier paper, and is a key ingredient for the comparison with stellar evolution models. These two developments motivate us to take a fresh look at the system in order to investigate the impact of the new measurements. Furthermore, Weber & Strassmeier (2011) have presented evidence that the orbit of Capella may be very slightly eccentric, unexpectedly, whereas all previous studies, including our own, assumed it is circular. It is of interest, therefore, to revisit our 2009 study of tidal evolution in the system (orbit circularization and rotational synchronization) with more sophisticated models than used there, especially in light of the new masses.

We have organized the paper as follows. In Section 2 we describe the new spectroscopic observations of Weber & Strassmeier (2011) and comment on the issue of systematics in

[5] Capella has a wide common proper motion companion that is itself a visual binary composed of M dwarfs. The system is therefore a hierarchical quadruple. Revised properties of the M dwarf pair are reported in the Appendix.

the radial velocities, in comparison with our previous results from 2009. A revised orbital fit for Capella is presented in Section 3, using also astrometric and other measurements from T09. Section 4 reports a new detailed chemical analysis of both stars from disentangled spectra, along with a determination of the atmospheric parameters. The revised physical properties of the stars are collected in Section 5, and are compared against three different sets of stellar evolution models in Section 6. Key chemical diagnostics available for Capella are also compared with model predictions in this section. Then in Section 7 we examine the evolution of orbital and stellar properties subjected to the influence of tidal mechanisms, as a test of that theory. Section 8 presents a discussion of the results and concluding remarks. Finally, the Appendix provides an update on the orbital properties of the wide common proper motion companion of Capella.

2. RADIAL VELOCITIES

The numerous historical radial-velocity (RV) measurements of Capella have been discussed at length in our T09 study, which highlighted how challenging it has been to determine accurate values for the rapidly rotating secondary star ($v \sin i \approx 35\,\mathrm{km\,s^{-1}}$), whereas those of the sharp-lined primary ($v \sin i \approx 4\,\mathrm{km\,s^{-1}}$) have been quite consistent over the last century. T09 presented 162 new RV determinations for both components based on spectra obtained at the CfA covering only a very narrow wavelength range (45 Å). The RVs were measured using the two-dimensional cross-correlation algorithm TODCOR (Zucker & Mazeh 1994), with synthetic templates appropriate for each star. Because of the limited wavelength coverage, those measurements are susceptible to systematic errors resulting mostly from lines shifting in and out of the spectral window as a function of orbital phase. Therefore, an effort was made to control those biases by performing numerical simulations to determine corrections to the velocities, which were at the level of the final uncertainties in the individual measurements for the secondary, and slightly larger for the primary. Final errors in the RVs as measured from the scatter in the orbital fit were about $0.44\,\mathrm{km\,s^{-1}}$ for the primary and $0.89\,\mathrm{km\,s^{-1}}$ for the secondary. A sign that systematic errors remained at some level in the CfA velocities was evident in the residuals of the secondary star shown in Figure 2 of T09, in which a pattern can be seen as a function of orbital phase, with a peak semi-amplitude of about twice the typical error. Possible explanations for this, as discussed by T09, include the presence of spots on the active secondary star, or template mismatch.[6] An additional indication of possible biases was the fact that a small offset ($0.267 \pm 0.079\,\mathrm{km\,s^{-1}}$) was found between the primary and secondary velocities in the global orbital fit of T09 that could not be accounted for by differences in the gravitational redshift between the stars, and was ascribed to similar reasons as the secondary residual pattern.

More recently Weber & Strassmeier (2011) have reported new RV measurements for Capella based on a very large set of more than 400 spectra obtained with the STELLA échelle spectrograph (Strassmeier et al. 2010) on a 1.2 m robotic telescope in Tenerife, Spain. These spectra are of far superior quality than those of T09, both in terms of wavelength coverage (two orders of magnitude larger) and signal-to-noise ratios (S/N). Weber & Strassmeier (2011) derived velocities using a similar two-dimensional cross-correlation approach as T09, and also performed numerical simulations to assess and correct for systematic errors caused by the measuring technique. The velocity scatter from their orbital fit is $0.064\,\mathrm{km\,s^{-1}}$ for the primary and $0.297\,\mathrm{km\,s^{-1}}$ for the secondary, seven and three times smaller than in T09, respectively. The key difference in this data set compared to T09 is in the resulting velocity semi-amplitude of the secondary star ($K_\mathrm{B} = 26.840 \pm 0.024\,\mathrm{km\,s^{-1}}$), which is more than 6σ larger than reported by T09 ($K_\mathrm{B} = 26.260 \pm 0.087\,\mathrm{km\,s^{-1}}$). This difference alone leads to absolute masses for Capella that are 4% larger than in T09 for the primary, and 2% larger for the secondary, a very significant change that exceeds the formal mass errors by a factor of many. The semi-amplitudes K_A of the primary star, on the other hand, are in virtually perfect agreement (see below).

Despite the much improved random errors of Weber & Strassmeier (2011), the residuals of the secondary velocities from their spectroscopic orbital model (see their Figure 2) still display a phase-dependent pattern reminiscent of the one in T09, also with a semi-amplitude of roughly twice the errors, but at a much lower level in absolute terms. Moreover, they noted that a small offset is seen again between the primary and secondary velocities ($0.059\,\mathrm{km\,s^{-1}}$) that cannot be explained by the gravitational redshift effect. This suggests that systematic errors may still be lurking in these new measurements, for possibly some of the same reasons as before. Nevertheless, any remaining systematics are likely to be significantly less important than in T09, as expected not only from the much higher quality of the spectroscopic material, but suggested also by the significantly smaller magnitudes of (i) the corrections for systematics applied by Weber & Strassmeier (2011), (ii) the formal uncertainties in the individual RVs, or equivalently, the scatter from the spectroscopic orbital solution, (iii) the amplitude of the residual pattern for the secondary, and (iv) the unexplained residual primary/secondary offset. In the next section we therefore incorporate these measurements in a new orbital analysis of Capella.

Of the 438 RV measurements reported in Table 1 of Weber & Strassmeier (2011), their final solution excluded 14 for the primary and 7 for the secondary. We have done the same here as we found them to give unusually large residuals, and we adopted also the measurement uncertainties as published.

3. REVISED ORBITAL FIT

The global orbital solution in our T09 study of Capella combined all usable astrometric observations in the literature with the CfA RVs for both stars, as well as radial velocities for the primary star from many of the historical data sets. The latter were carefully examined to ensure that they imply K_A values consistent with those from the CfA RVs in separate spectroscopic solutions using the same fixed orbital period (see T09, Table 2). A similar solution of the Weber & Strassmeier (2011) velocities shows that the primary semi-amplitude, $K_\mathrm{A} = 29.959 \pm 0.005\,\mathrm{km\,s^{-1}}$, is essentially the same as that from the CfA RVs, $K_\mathrm{A} = 29.96 \pm 0.04\,\mathrm{km\,s^{-1}}$. Therefore, for our revised global solution below we have incorporated the Weber & Strassmeier (2011) measurements for both stars, the

[6] In particular, due to limitations in the available library of synthetic spectra they used, the macroturbulent velocity of the templates ($\zeta_\mathrm{RT} = 1.5\,\mathrm{km\,s^{-1}}$) was not quite as large as appropriate for giant stars. This also resulted in an overestimation of the rotational velocities of the components, as discussed by T09.

CfA velocities for the primary (but not the secondary), and the primary velocities from the same historical data sets as used in T09. Although the Weber & Strassmeier (2011) observations certainly dominate by weight, the older measurements are still useful because they extend the baseline more than a century, improving the orbital period.

The extensive astrometry available for Capella includes measurements made by many authors with the technique of long-baseline interferometry, beginning with the work of Merrill (1922), as well as speckle interferometry, direct imaging, and the intermediate astrometric measurements from *Hipparcos*. These have all been described and tabulated in our earlier study, and we refer the reader to that work for details. So far as we are aware, no further astrometric observations have been published for Capella except for those of Huby et al. (2013), which we do not use here, however, because of concerns expressed by these authors about possible systematic errors affecting their measurements.

Our global orbital fit follows closely that described by T09, and includes the following parameters: orbital period ($P_{\rm orb}$), relative angular semimajor axis (a''), inclination angle ($i_{\rm orb}$), eccentricity (e), longitude of periastron of the more massive and cooler star ($\omega_{\rm A}$)[7], position angle of the ascending node for the equinox J2000.0 ($\Omega_{\rm J2000}$), time of periastron passage ($T_{\rm peri}$), center-of-mass velocity (γ), the velocity semi-amplitudes for each star ($K_{\rm A}$ and $K_{\rm B}$), the angular semimajor axis of the photocenter ($a''_{\rm phot}$), corrections to the *Hipparcos* catalog values of the sky position of the barycenter ($\Delta\alpha\cos\delta$, $\Delta\delta$) at the mean catalog reference epoch of 1991.25, and corrections to the proper motion components ($\Delta\mu_{\alpha}\cos\delta$, $\Delta\mu_{\delta}$). To account for differences in the zero points of the various RV data sets relative to the primary star measurements of Weber & Strassmeier (2011), we have also solved for 10 velocity offsets, one for each set. An additional parameter, f_{ρ}, was included to correct the scale of the angular separation measurements from two of the astrometric data sets (see T09 for details).

Weber & Strassmeier (2011) discussed several adjustments made to their secondary velocities to place them on the same system as their primary velocities of Capella. These adjustments were intended to correct for differences in the gravitational redshift of the two components, and other shifts of unknown origin (see above). From their discussion it is not entirely clear to us whether these constant shifts have been applied to the velocities they reported, so our global solution includes one additional offset, $\Delta_{\rm AB}$, to account for possible residual effects. With this, the total number of adjustable parameters in our fit is 27.

The solution in our T09 study assumed a circular orbit for Capella, as have all previous analyses of the binary. We noted, however, that there were hints of a non-zero eccentricity in the interferometric measurements of Hummel et al. (1994), though not in the CfA RVs or in any of the other data sets. We ascribed this to the transformation that Hummel et al. (1994) made between their original interferometric visibilities (V^2) and the nightly relative positions in polar coordinates that they published, given that their own solution using the original visibilities indicated a circular orbit. As pointed out by Weber & Strassmeier (2011), however, a spectroscopic fit using their RVs also indicates a statistically significant non-zero eccentricity, of very nearly the same magnitude as we had seen, and even with a consistent longitude of periastron. This suggests we may have been too quick to dismiss the possibility of a non-circular orbit in T09, as unexpected as this may be for a pair of giants (one being a clump star) in a period of 104 days (see, e.g., Massarotti et al. 2008). We discuss this further in Section 7. For our new global solution we have chosen to allow the orbit to be eccentric, on the assumption that the effect is real.

The parameters of our fit are presented in Table 1, along with other properties derived directly from the orbital elements. With the exception of $K_{\rm B}$ and the quantities that depend on it, the other results are rather similar to those in T09. The eccentricity is essentially the same as derived by Weber & Strassmeier (2011).

4. SPECTROSCOPIC ANALYSIS

Until recently the only detailed chemical analysis available for Capella was that by McWilliam (1990), indicating a sub-solar composition of [Fe/H] $= -0.37 \pm 0.22$ on the scale of Grevesse (1984), equivalent to [Fe/H] $= -0.20 \pm 0.22$ on a more modern scale in which the solar iron abundance is A(Fe) $= 7.50$.[8] This determination is presumably based on the sharp lines of the primary star, but there is no indication that the presence in the spectrum of the nearly equally bright secondary was properly accounted for, and in addition, the analysis adopted an incorrect primary temperature. A new metallicity determination was reported by Fuhrmann (2011) that gives a rather higher abundance of [Fe/H] $= +0.05 \pm 0.08$, apparently on the scale of Grevesse et al. (1996) in which the solar iron abundance is also A(Fe) $= 7.50$. This study is based on spectral synthesis applied to eight Fe I lines and one Fe II line from a single composite spectrum with some degree of line blending, using an unspecified primary/secondary flux ratio.

Below we describe our new determination of the chemical composition and atmospheric parameters of Capella based on the technique of spectral disentangling (Simon & Sturm 1994), which bypasses the line blending problems inherent in previous analyses that used composite spectra.

4.1. Disentangling

For our spectroscopic analysis we made use of public archival spectra taken in 2003 and 2004 with the ELODIE spectrograph (Baranne et al. 1996) on the 1.93 m telescope at the Observatoire de Haute-Provence, in France. The nominal resolving power of the instrument is $R = 42{,}000$, and the 15 spectra used span the approximate wavelength range 4000–6800 Å, with S/N ranging from about 130 to 560 per pixel at 5550 Å. We have disentangled these spectra using the FDBinary program of Ilijić et al. (2004), in the same way as described recently by Torres et al. (2014). FDBinary implements spectral disentangling in the Fourier domain according to Hadrava (1995). The S/N of the resulting disentangled spectra are approximately 510 for the cooler primary and 590 for the secondary. Renormalization of the disentangled spectra for a proper abundance analysis (see Pavlovski & Hensberge 2005; Lehmann et al. 2013) requires

[7] Note that this is the fainter star at optical wavelengths (see T09), which we refer to as star "A."

[8] We use the standard abundance notation in which A(X)= $\log[n(\mathrm{X})/n(\mathrm{H})] + 12$, where $n(\mathrm{X})$ and $n(\mathrm{H})$ are the numbers of atoms per unit volume of element X and of hydrogen.

Table 1
Revised Orbital Solution for Capella

Parameter	Value
Adjusted quantities	
$P_{\rm orb}$ (days)	104.02128 ± 0.00016
a'' (mas)	56.442 ± 0.023
$i_{\rm orb}$ (deg)	137.156 ± 0.046
e	0.00089 ± 0.00011
$\omega_{\rm A}$ (deg)	342.6 ± 9.0
$\Omega_{\rm J2000}$ (deg)	40.522 ± 0.039
$T_{\rm peri}$ (HJD−2,400,000)	48147.6 ± 2.6
γ (km s^{-1})[a]	+29.9387 ± 0.0032
$K_{\rm A}$ (km s^{-1})	25.9611 ± 0.0044
$K_{\rm B}$ (km s^{-1})	26.860 ± 0.017
$a''_{\rm phot}$ (mas)	2.14 ± 0.70
$\Delta\alpha^*$ (mas)	−0.53 ± 0.81
$\Delta\delta$ (mas)	−0.37 ± 0.57
$\Delta\mu_{\ell_\alpha}\cos\delta$ (mas yr^{-1})	+0.33 ± 1.00
$\Delta\mu_\delta$ (mas yr^{-1})	−0.04 ± 0.60
f_ρ[b]	1.0400 ± 0.0032
$\Delta_{\rm AB}$ for WS (km s^{-1})[c]	+0.050 ± 0.013
Δ_1 ⟨WS−C01⟩ (km s^{-1})	−0.19 ± 0.14
Δ_2 ⟨WS−N00⟩ (km s^{-1})	+2.35 ± 0.45
Δ_3 ⟨WS−G08⟩ (km s^{-1})	−0.67 ± 0.26
Δ_4 ⟨WS−S39⟩ (km s^{-1})	−1.52 ± 0.16
Δ_5 ⟨WS−S53⟩ (km s^{-1})	+0.62 ± 0.14
Δ_6 ⟨WS−B86⟩ (km s^{-1})	−0.10 ± 0.13
Δ_7 ⟨WS−S90⟩ (km s^{-1})	−2.07 ± 0.60
Δ_8 ⟨WS−B91⟩ (km s^{-1})	−0.62 ± 0.13
Δ_9 ⟨WS−B93⟩ (km s^{-1})	+0.79 ± 0.10
Δ_{10} ⟨WS−T09⟩ (km s^{-1})	+0.289 ± 0.035
Derived quantities	
$M_{\rm A}$ ($M_\odot$)	2.5687 ± 0.0074
$M_{\rm B}$ ($M_\odot$)	2.4828 ± 0.0067
$q \equiv M_{\rm B}/M_{\rm A}$	0.96653 ± 0.00062
a (10^6 km)	111.11 ± 0.10
a ($R_\odot$)	159.72 ± 0.15
a (AU)	0.74272 ± 0.00069
$\pi_{\rm orb}$ (mas)	75.994 ± 0.089
Distance (pc)	13.159 ± 0.015
$\mu_{\ell_\alpha}\cos\delta$ (mas yr^{-1})	+75.85 ± 1.00
μ_δ (mas yr^{-1})	−427.17 ± 0.60
$(\ell_{\rm B}/\ell_{\rm A})_{H_p}$[d]	1.204 ± 0.060

Notes. References for the RV offsets Δ_1 to Δ_{10} are: C01 = Campbell (1901); N00 = Newall (1900); G08 = Goos (1908); S39 = Struve (1939); S53 = Struve & Kilby (1953); B86 = Beavers & Eitter (1986); S90 = Shcherbakovet al. (1990); B91 = Batten et al. (1975); B93 = Barlow et al. (1993); and T09 = Torres et al. (2009). The physical constants used in the analysis are those specified by Torres et al. (2010).
[a] On the reference frame of the RVs of Weber & Strassmeier (2011).
[b] Scale factor for the angular separation measurements by Merrill (1922) and Kulagin (1970).
[c] Primary/secondary offset for the Weber & Strassmeier (2011) velocities (WS), in the sense ⟨primary *minus* secondary⟩.
[d] Flux ratio between the secondary and primary in the *Hipparcos* passband, derived from the angular semimajor axis, the semimajor axis of the photocentric orbit as measured by the satellite, and the velocity semi-amplitudes (see T09).

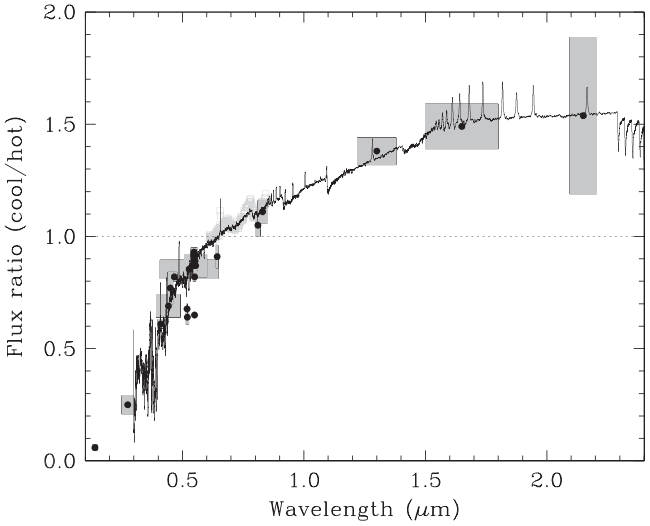

Figure 1. Measured flux ratios for the components of Capella (cool star relative to hot star, i.e., primary relative to secondary). Values from T09 are indicated with dots and error boxes, in which the horizontal length of each box indicates the wavelength coverage. Other measurements from Huby et al. (2013) are shown by the lighter gray squares in the range 0.611–0.843 μm. Overplotted is the predicted flux ratio based on synthetic spectra by Husser et al. (2013) scaled according to the radius ratio given by T09.

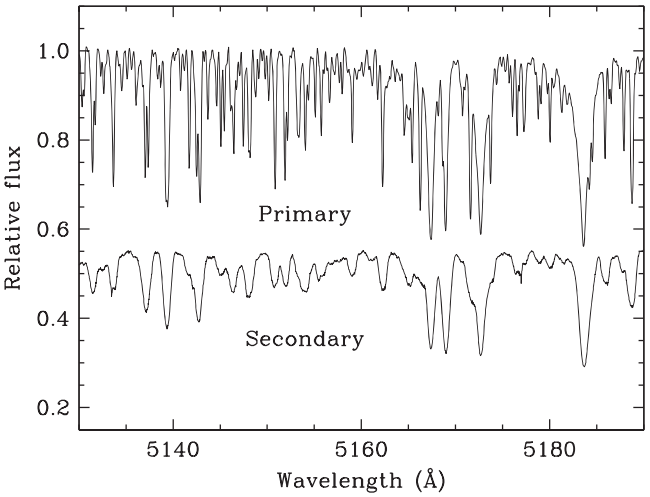

Figure 2. Portions of the disentangled ELODIE spectra of Capella. Secondary shifted vertically for clarity.

knowledge of the relative flux contribution of each star at each wavelength. Flux ratios for Capella have been measured throughout the UV, optical, and near-infrared range, as reported by T09. Figure 1 shows the predicted flux ratio based on PHOENIX model spectra from Husser et al. (2013) for parameters near those of the components, along with the measurements tabulated by T09 as well as others from the recent study by Huby et al. (2013) over the range 6112–8430 Å. The agreement is very good. For our purposes we have used a smoothed version of this relation. Sample segments of the disentangled spectra of the two components of Capella are presented in Figure 2.

4.2. Atmospheric Parameters and Abundance Analysis

The general methodology for determining the atmospheric parameters and abundances from the disentangled spectra

follows the procedures described by Torres et al. (2014). The UCLSYN code (Smalley et al. 2001) was used to synthesize spectra, based on initial temperatures and surface gravities from T09 and a built-in grid of LTE model atmospheres by Castelli & Kurucz (2003) with a scaled-solar mixture. Line broadening was modeled adopting an initial composition matching the Sun, and microturbulent velocities of $\xi_t = 1.5\,\mathrm{km\,s^{-1}}$ for both components (fine-tuned below). Least-squares fitting then yielded a macroturbulent velocity for the primary of $\zeta_A = 6.6 \pm 0.4\,\mathrm{km\,s^{-1}}$, and a projected rotational velocity of $v_A \sin i = 4.4 \pm 0.5\,\mathrm{km\,s^{-1}}$. Given the rapid rotation of the secondary, macroturbulence has a negligible effect on the line profiles and we made no attempt to determine it from the ELODIE spectra. The rotational velocity of the companion was measured to be $v_B \sin i = 34.5 \pm 0.7\,\mathrm{km\,s^{-1}}$.

Elemental abundances were determined using spectral lines suitable for giant stars over the wavelength range 4600–6750 Å. Line lists and atomic data were taken from the work of Reddy et al. (2012), Böcek Topcu et al. (2015), and Lyubimkov et al. (2015). Equivalent widths measured within UCLSYN for the very numerous iron lines were used to set the microturbulent velocities from the condition of a null correlation between the abundance and the reduced equivalent widths. We derived values of $\xi_{t,A} = 1.48 \pm 0.08\,\mathrm{km\,s^{-1}}$ for the primary and $\xi_{t,B} = 1.55 \pm 0.11\,\mathrm{km\,s^{-1}}$ for the secondary. We also made an estimate of the effective temperatures from the usual condition of excitation equilibrium, iterating with the measurement of ξ_t, with the following results: $T_{\rm eff,A} = 4980 \pm 80$ K and $T_{\rm eff,B} = 5750 \pm 110$ K. There is very good agreement between these values and others reported by T09; we discuss them further below. The surface gravities in our analysis were held fixed at the estimates reported by T09, which are very close to our final values described in the next section.

Detailed abundances were determined for 22 species in both stars, and oxygen in the primary only. They are listed in Table 2, which includes also the values relative to the Sun on the scale of Asplund et al. (2009). No adjustments have been applied for NLTE effects. The uncertainties account for possible errors in $T_{\rm eff}$ as reported above, and also include a contribution from a representative error of $0.1\,\mathrm{km\,s^{-1}}$ in ξ_t. The uncertainties in $\log g$ have a negligible impact. The choice of the mixture adopted in the model atmospheres, particularly the CNO composition, also has a minimal effect on our abundance determinations (see also Morel et al. 2014). We find no dependence of the Fe abundance on wavelength, which is an indication that our adopted wavelength-dependent flux ratios (Figure 1) are accurate and do not introduce significant systematic errors in the abundances. A further indication of the robustness of our determinations is the fact that the abundances are quite similar for the two components (except for species affected by evolution; see below), as expected for a binary system.

The weighted average iron abundance of the two stars from Fe I is $[\mathrm{Fe/H}] = -0.04 \pm 0.06$, or very nearly solar, in contrast with the sub-solar composition adopted by T09, and in better agreement with the estimate by Fuhrmann (2011). We find no significant enhancement of the α elements in Capella: $[\alpha/\mathrm{Fe}] = -0.02 \pm 0.04$. A graphical representation of the abundance pattern for the two components is seen in Figure 3, compared to the solar composition.

The lithium abundance has long been known to be very different for the two components of this binary (Wallerstein 1964, 1966) as a result of chemical evolution in the primary. We used spectral lines and atomic data from Lyubimkov et al. (2012) in the vicinity of the Li I λ6708 doublet to make new estimates for each star, and obtained values of $\mathrm{A(Li)} = 1.08 \pm 0.11$ and $\mathrm{A(Li)} = 3.28 \pm 0.13$ for the primary and secondary, respectively. These are consistent with previous measurements. The equivalent widths we determined are 21.4 ± 0.7 and 297.4 ± 8.0 mÅ.

Additional chemical diagnostics for Capella have been reported by T09, and include the $^{12}\mathrm{C}/^{13}\mathrm{C}$ carbon isotope ratio for the primary star (27 ± 4; Tomkin et al. 1976) and the C/N abundance ratios for both components (0.57 ± 0.06 for the primary and 3.30 ± 0.16 for the secondary). We adopt those as published.

5. PHYSICAL PROPERTIES

The revised masses of Capella that incorporate the new RVs of Weber & Strassmeier (2011) have formal uncertainties of 0.3%, and differ only slightly from theirs through a combination of a marginally larger K_B value in our analysis and a smaller orbital inclination angle than they used. The new masses are 4.2% and 1.6% larger than those listed by T09, which is a significant difference due almost entirely to the change in the velocity semiamplitude of the secondary. The radii, based on the individual angular diameters from T09 and the revised orbital parallax, are approximately 0.9% larger than before, and have precisions of about 5% and 4% for the primary and secondary, respectively. These are limited by the angular diameters, as the uncertainty in the orbital parallax is only 0.11%.

T09 reported three independent estimates of the effective temperatures for the two components. One is from a comparison of their spectroscopic observations with synthetic spectra with solar metallicity, giving $T_{\rm eff,A} = 4900 \pm 100$ K and $T_{\rm eff,B} = 5710 \pm 100$ K. Another came from the use of the measured angular diameters of the stars along with their apparent magnitudes, the parallax, and bolometric corrections. Slightly revised values for those temperatures are $T_{\rm eff,A} = 4970 \pm 160$ K and $T_{\rm eff,B} = 5690 \pm 130$ K. A third determination by T09 was based on the measured color indices for the stars, and the use of the color/temperature calibrations of Ramírez & Meléndez (2005), which depend on metallicity. A sub-solar composition $[\mathrm{m/H}] = -0.37 \pm 0.07$ had been assumed by T09, whereas we now derive a value much closer to solar. Using our determination of $[\mathrm{Fe/H}] = -0.04 \pm 0.06$ (Section 4.2), the revised photometric estimates become 4940 and 5680 K, which are 30 and 70 K higher than before. Furthermore, a careful examination of the zero point of the Ramírez & Meléndez (2005) calibrations by Casagrande (2010) suggests that the scale of those relations is too cool by about 85 K compared to the best available absolute scale, at least in the temperature range of the Capella components. We have therefore applied this offset, obtaining corrected photometric estimates of $T_{\rm eff,A} = 5025 \pm 110$ K and $T_{\rm eff,B} = 5765 \pm 120$ K. The uncertainties include a contribution of 100 K added in quadrature to the photometric and calibration errors, to be conservative. Finally, a fourth temperature determination was reported in the previous section from the disentangled ELODIE spectra, giving $T_{\rm eff,A} = 4980 \pm 80$ K and $T_{\rm eff,B} = 5750 \pm 110$ K. The

Table 2
Abundances from our Disentangled ELODIE Spectra of Capella

		Primary			Secondary			
A	X	Abundance	[X/H]	*N*	Abundance	[X/H]	*N*	log $\epsilon_\odot$
3	Li I	1.08 ± 0.11	−0.07 ± 0.15	3	3.28 ± 0.13	+2.30 ± 0.16	3	1.05 ± 0.10
6	C I	8.25 ± 0.14	−0.18 ± 0.15	4	8.28 ± 0.11	−0.15 ± 0.12	5	8.43 ± 0.05
8	O I	8.55 ± 0.11	−0.14 ± 0.12	1	...	...	...	8.69 ± 0.05
11	Na I	6.13 ± 0.09	−0.11 ± 0.10	4	6.33 ± 0.07	+0.09 ± 0.08	4	6.24 ± 0.04
12	Mg I	7.60 ± 0.09	+0.00 ± 0.10	2	7.42 ± 0.10	−0.18 ± 0.11	5	7.60 ± 0.04
14	Si I	7.69 ± 0.04	+0.18 ± 0.05	10	7.59 ± 0.07	+0.08 ± 0.08	7	7.51 ± 0.03
20	Ca I	6.27 ± 0.11	−0.07 ± 0.12	8	6.38 ± 0.11	+0.04 ± 0.08	7	6.34 ± 0.04
21	Sc I	3.13 ± 0.15	−0.02 ± 0.16	5	3.16 ± 0.10	+0.01 ± 0.11	6	3.15 ± 0.04
21	Sc II	3.12 ± 0.07	−0.03 ± 0.08	8	3.10 ± 0.08	−0.05 ± 0.09	11	3.15 ± 0.04
22	Ti I	4.96 ± 0.12	+0.01 ± 0.13	15	5.02 ± 0.09	+0.07 ± 0.10	11	4.95 ± 0.05
22	Ti II	4.93 ± 0.05	−0.02 ± 0.07	3	4.91 ± 0.09	−0.04 ± 0.10	6	4.95 ± 0.05
23	V I	4.07 ± 0.12	+0.14 ± 0.14	14	4.10 ± 0.07	+0.17 ± 0.11	13	3.93 ± 0.08
24	Cr I	5.64 ± 0.09	+0.00 ± 0.10	9	5.67 ± 0.07	+0.03 ± 0.08	11	5.64 ± 0.04
24	Cr II	5.61 ± 0.09	−0.03 ± 0.10	7	5.57 ± 0.07	−0.07 ± 0.08	6	5.64 ± 0.04
25	Mn I	5.32 ± 0.09	−0.11 ± 0.05	8	5.31 ± 0.08	−0.12 ± 0.09	5	5.43 ± 0.05
26	Fe I	7.47 ± 0.06	−0.03 ± 0.07	42	7.44 ± 0.08	−0.06 ± 0.09	41	7.50 ± 0.04
26	Fe II	7.39 ± 0.07	−0.11 ± 0.08	8	7.38 ± 0.06	−0.12 ± 0.07	11	7.50 ± 0.04
27	Co I	4.87 ± 0.08	−0.12 ± 0.10	8	5.03 ± 0.07	+0.04 ± 0.10	5	4.99 ± 0.07
28	Ni I	6.20 ± 0.04	−0.02 ± 0.06	16	6.21 ± 0.07	−0.01 ± 0.08	17	6.22 ± 0.04
39	Y II	2.11 ± 0.09	−0.10 ± 0.10	4	2.23 ± 0.05	+0.02 ± 0.07	5	2.21 ± 0.05
40	Zr I	2.54 ± 0.07	−0.04 ± 0.08	5	2.25 ± 0.12	−0.33 ± 0.13	3	2.58 ± 0.04
57	La II	1.11 ± 0.08	+0.01 ± 0.09	5	1.23 ± 0.05	+0.13 ± 0.06	5	1.10 ± 0.04
60	Nd II	1.49 ± 0.06	+0.07 ± 0.07	8	1.52 ± 0.05	+0.10 ± 0.06	7	1.42 ± 0.04

Note. Columns list the atomic number, the element and ionization degree, the logarithm of the number abundance on the usual scale in which A(H) = 12, the logarithmic abundance relative to the Sun, and the number of spectral lines measured. The last column gives the reference photospheric solar values from Asplund et al. (2009).

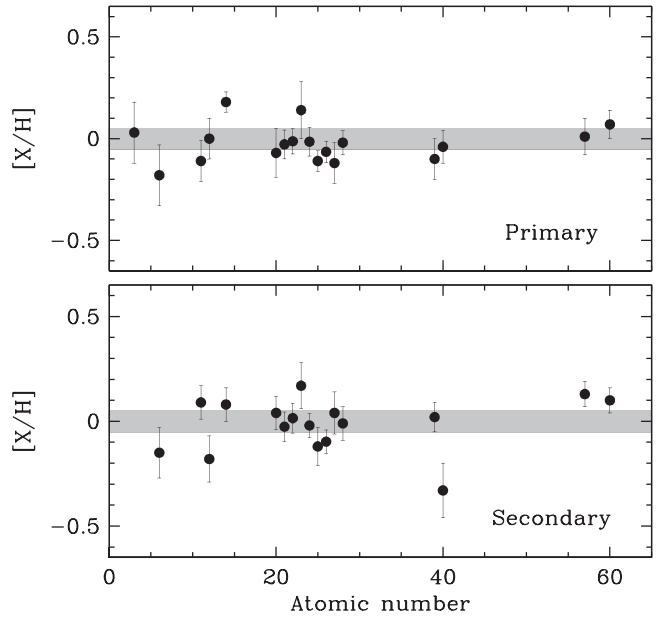

Figure 3. Photospheric abundance pattern measured for the Capella components, compared to the standard solar composition of Asplund et al. (2009; gray shading). Abundances from different ions of the same element have been averaged.

weighted averages of the four values for each component are $T_{\rm eff,A} = 4970 \pm 50$ K and $T_{\rm eff,B} = 5730 \pm 60$ K, in which the uncertainties account not only for the individual weights but also for the scatter of the measurements, and are believed to be realistic. These averages are 50 K hotter than in T09.

The available determinations of $v \sin i$ for both components were summarized in our previous work (T09, Table 14). Our present measurements from the ELODIE spectra are consistent with those of others, as well as with the measurements reported by Fuhrmann (2011), which are $v_{\rm A} \sin i = 3.5 \pm 0.8$ km s^{-1} and $v_{\rm B} \sin i = 35.4 \pm 3.2$ km s^{-1}. The weighted averages of all independent determinations (5 for the primary, 10 for the secondary) that have taken account of macroturbulence broadening, especially for the primary component, are $v_{\rm A} \sin i = 4.1 \pm 0.4$ km s^{-1} and $v_{\rm B} \sin i = 35.0 \pm 0.5$ km s^{-1}, which we adopt for the remainder of the paper.

The masses, radii, temperatures, and other derived properties are summarized in Table 3. Note that the bolometric luminosities are independent of the temperatures and radii, and are based on the apparent magnitudes, the orbital parallax, and bolometric corrections from Flower (1996), as in T09. If we instead compute them from $T_{\rm eff}$ and R, the results are consistent, but have larger formal uncertainties: $L_{\rm A} = 78.7 \pm 8.1\ L_\odot$ and $L_{\rm B} = 75.4 \pm 6.4\ L_\odot$.

6. COMPARISON WITH STELLAR EVOLUTION MODELS

Up until now the ability of stellar evolution models to match all of the global properties of both components of Capella simultaneously at a single age has not been entirely satisfactory, likely at least in part because there are so many observational constraints available. This has made it difficult to establish the evolutionary status of the primary star unambiguously, although it has widely been thought to be a core helium-burning (clump) star, based on timescale arguments (see T09). The significantly different (and more precise) masses obtained above, and evidence that the chemical composition is rather

Table 3
Revised Physical Parameters of Capella

Parameter	Primary	Secondary
Mass ($M_\odot$)	2.5687 ± 0.0074	2.4828 ± 0.0067
$q \equiv M_B/M_A$	0.96653 ± 0.00062	
a (10^6 km)	111.11 ± 0.10	
a (AU)	0.74272 ± 0.00069	
π_{orb} (mas)	75.994 ± 0.089	
Distance (pc)	13.159 ± 0.015	
Radius ($R_\odot$)	11.98 ± 0.57	8.83 ± 0.33
log g (cgs)	2.691 ± 0.041	2.941 ± 0.032
T_{eff} (K)	4970 ± 50	5730 ± 60
Luminosity ($L_\odot$)[a]	78.7 ± 4.2	72.7 ± 3.6
BC_V (mag)	−0.304 ± 0.055	−0.089 ± 0.051
M_V (mag)	0.296 ± 0.016	0.167 ± 0.015
$v \sin i$ (km s^{-1})[b]	4.1 ± 0.4	35.0 ± 0.5
P_{rot} (days)[c]	104 ± 3	8.5 ± 0.2
Age (Myr)[d]	590–650	
[Fe/H]	−0.04 ± 0.06	
A(Li)	1.08 ± 0.11	3.28 ± 0.13
$^{12}C/^{13}C$ [e]	27 ± 4	...
C/N [c]	0.57 ± 0.06	3.30 ± 0.16

Notes.
[a] Computed from V, π_{orb}, and BC_V from Flower (1996), adopting $M_{bol}^\odot = 4.732$ (see T09 and Torres 2010).
[b] Average of 5 measurements from the literature for the primary and 10 for the secondary that account for macroturbulence, including our own (see text).
[c] Measured values adopted from T09.
[d] Age range from the MESA and Granada models (see the text).
[e] Measurement by Tomkin et al. (1976).

different from that previously assumed, motivate us to revisit the comparison with stellar evolution models here.

An initial test was made using the PARSEC isochrones of Bressan et al. (2012).[9] These models adopt the solar distribution of heavy elements from the compilation by Grevesse & Sauval (1998), with adjustments to some elements following Caffau et al. (2011) such that the solar photospheric metallicity is $Z_\odot = 0.01524$. On this scale the measured abundance of Capella (Section 4.2) corresponds approximately to $Z = 0.0133$. The helium abundance Y follows an adopted enrichment law with a slope $\Delta Y/\Delta Z = 1.78$, which results in a value for Capella of $Y = 0.272$. Convection is treated in the standard mixing length theory approximation. The calibration to the Sun leads to a mixing length parameter of $\alpha_{MLT} = 1.74$, which is held fixed in these models. Convective core overshooting is also included, with an efficiency parameter of $\Lambda_c = 0.5$ for Capella, representing the mean free path of convective bubbles across the border of the convective region, expressed in units of the pressure scale height H_p. This is roughly equivalent to $\alpha_{ov} = 0.25$ pressure scale heights above the convective boundary in the more commonly used formulation of this phenomenon (see below). Mass loss from stellar winds is not considered in these models for the mass range of interest for Capella, nor is rotation.

With the chemical composition and convective parameters fixed as described above, we searched for the common age giving the best fit to the masses, radii, temperatures, and

[9] http://stev.oapd.inaf.it/cmd

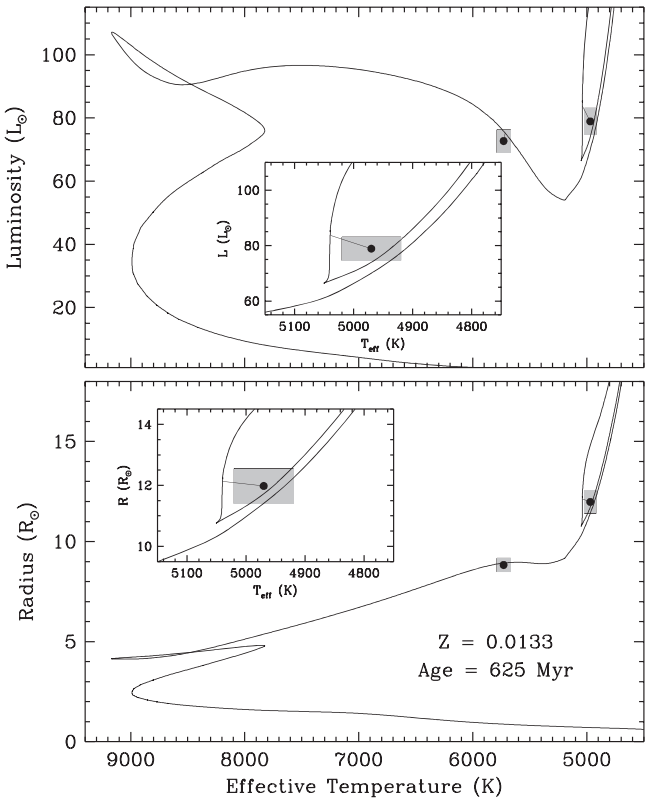

Figure 4. Comparison of the observed properties of Capella (M, R, T_{eff}, L, q) with a PARSEC isochrone from the model series by Bressan et al. (2012) in the L–T_{eff} and R–T_{eff} planes. Metallicity and age are as indicated in the lower panel. The insets show enlargements around the primary star, with a short line segment connecting the measured location in each plane with the best-fit position along the isochrone. Corresponding insets for the secondary are not shown as the match to its properties is better.

luminosities of both stars using the χ^2 statistic

$$\chi^2 = \sum \left(\left[\frac{\Delta M}{\sigma_M}\right]^2 + \left[\frac{\Delta T_{eff}}{\sigma_{T_{eff}}}\right]^2 + \left[\frac{\Delta L}{\sigma_L}\right]^2 + \left[\frac{\Delta R}{\sigma_R}\right]^2 \right)$$

as the figure of merit, where the sum is over both stars and the Δ quantities represent the difference between the predicted and measured properties. A reasonably good fit was obtained for an age of 622 Myr, matching the properties of the stars within about 1.4 times their uncertainties, with the largest discrepancy being in the primary temperature. We note, however, that the mass ratio of Capella is known much more precisely than the individual masses, with $\sigma_q \approx 0.06\%$ compared to mass errors σ_M of 0.29% and 0.27%. The masses in the above fit were allowed to vary independently, and as a result the best-fit mass ratio differs from the measured value by about 3σ. We therefore repeated the fit constraining q to be near its measured value by using a corresponding penalty term $[\Delta q/\sigma_q]^2$ in χ^2 instead of the secondary mass term. We obtained a solution of similar quality (all properties reproduced within 1.4σ) and nearly the same age of 625 Myr. This fit is illustrated in Figure 4, and it places the primary star in the core helium-burning phase (clump).

Aside from the global structural properties of the stars considered above, several chemical diagnostics including the

lithium abundance, the C/N ratios, and the isotopic carbon abundance ratio $^{12}C/^{13}C$ are available for Capella that are not normally tabulated with published stellar evolution models, but that are nevertheless interesting to compare with theoretical predictions. To that end, we have performed an additional test against a second set of models by Claret (2004), occasionally referred to below as the Granada models.

These models adopt also the solar abundance distribution by Grevesse & Sauval (1998), with some adjustments such that the solar metallicity becomes $Z_\odot = 0.0189$. The abundance of Capella then corresponds approximately to $Z = 0.0172$, which we held fixed. The enrichment law $\Delta Y/\Delta Z = 2.0$ typically used in these models results in a helium abundance for Capella of $Y = 0.274$, similar to that used above. The solar-calibrated value of the mixing length parameter is $\alpha_{\rm MLT} = 1.68$, and convective core overshooting $\alpha_{\rm ov}$ is parametrized such that the mean free path above the convective boundary is $d_{\rm ov} = \alpha_{\rm ov} H_{\rm p}$. Rotation was initially not included in our tests.

A grid of Granada evolutionary tracks was computed for the measured masses and a range of convective parameters for each component of Capella, as in principle there is no reason to expect stars in such different evolutionary states to have the same convective properties. We varied $\alpha_{\rm MLT}$ between values of 1.0 and 2.2 in steps of 0.1, and $\alpha_{\rm ov}$ over the range 0.15–0.40, with a step of 0.05. Mass loss was included in these calculations following the prescription by Reimers (1975). Preliminary tests indicated a minimal loss of mass for both stars up to the present age, but we nevertheless incremented the initial values slightly by 0.005 $M_\odot$ and 0.002 $M_\odot$, respectively, so as to reproduce the measured masses exactly at the best-fit age. An excellent fit to the radii, temperatures, and luminosities of both stars was found for mixing length parameters of 1.80 for the primary and 1.50 for the secondary, and convective core overshooting parameters of 0.35 and 0.30, respectively, with estimated uncertainties in each of these of about 0.05. Deviations in R, $T_{\rm eff}$, and L from the measured values are all smaller than 0.4σ. The best-fit age we obtained, about 649 Myr, was constrained to be the same for the two stars. We illustrate this solution in Figures 5 and 6 for the L–$T_{\rm eff}$ and R–$T_{\rm eff}$ diagrams, respectively.

We point out that the age in this best-fit solution is driven entirely by the properties of the secondary, specifically, by its effective temperature. This is because that star is in such a rapid phase of evolution that the temperature is predicted to change drastically (by many times the observational uncertainty) in just 1 Myr. Figures 5 and 6 show, for example, that between the ages of 648 and 649 Myr the temperature of the secondary decreases by 1130 K, cooling by a further 660 K over the next million years. The primary, on the other hand, stays at essentially the same temperature over this time, and only changes its radius and luminosity, but at a much slower pace (see top insets in the figures). Consequently, it does not constrain the age nearly as much. Because of the rapid evolution of the secondary, the formal uncertainty in the age that comes from its temperature error is negligible. A more meaningful uncertainty may be obtained by varying its mass within allowed limits, which results in an age range of approximately ±5 Myr. This does not include possible systematic errors having to do with the physics in the models. As found above from the PARSEC models, the primary star is seen to be located in the clump, on the hot side of the giant loop

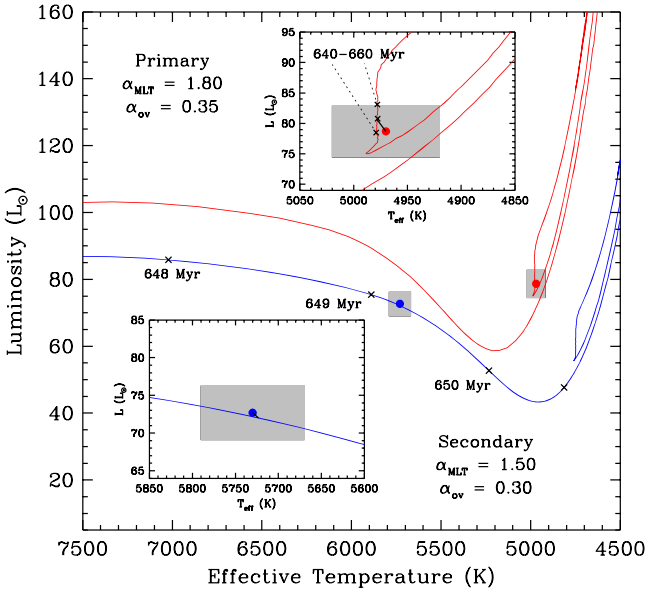

Figure 5. Comparison of the observed properties of Capella (dots and error boxes) with the Granada models by Claret (2004) in the L–$T_{\rm eff}$ diagram. The evolutionary tracks shown are for the measured masses (incremented by 0.005 $M_\odot$ for the primary and 0.002 $M_\odot$ for the secondary, to account for mass loss; see the text) and the measured metallicity ($Z = 0.0172$ for these models). Reference ages are marked along the secondary track, and the insets show enlargements around the position of each star, with a short line segment connecting the observations to the predicted positions.

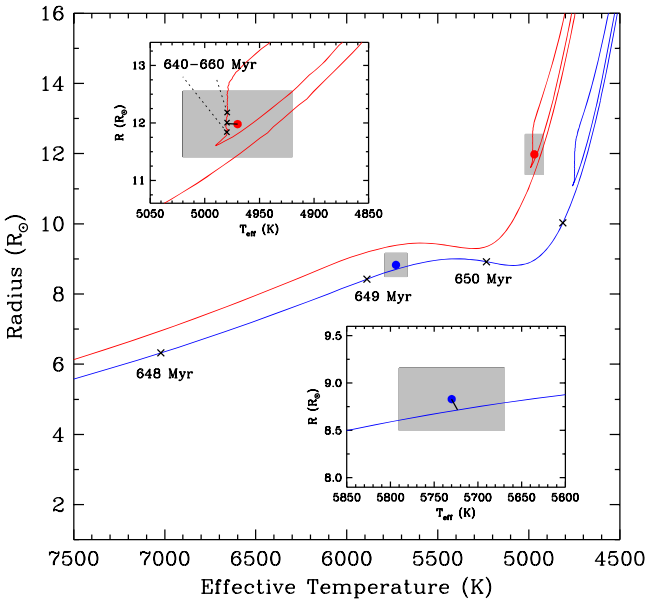

Figure 6. Similar to Figure 5 for the R–$T_{\rm eff}$ plane.

(end of the core helium-burning phase), where the radius and luminosity are increasing with time.

A test with Granada models that include rotation for both components gave a very similar fit, with an age of 655 Myr that is only marginally older than before.

The evolution of the surface chemistry in giants is the result of mixing and is directly related to the depth of the convection zone, which changes drastically as the stars approach the so-called first dredge-up, during their initial ascent of the giant branch. Other changes can occur later. The first dredge-up event is illustrated in Figure 7, which shows predictions from

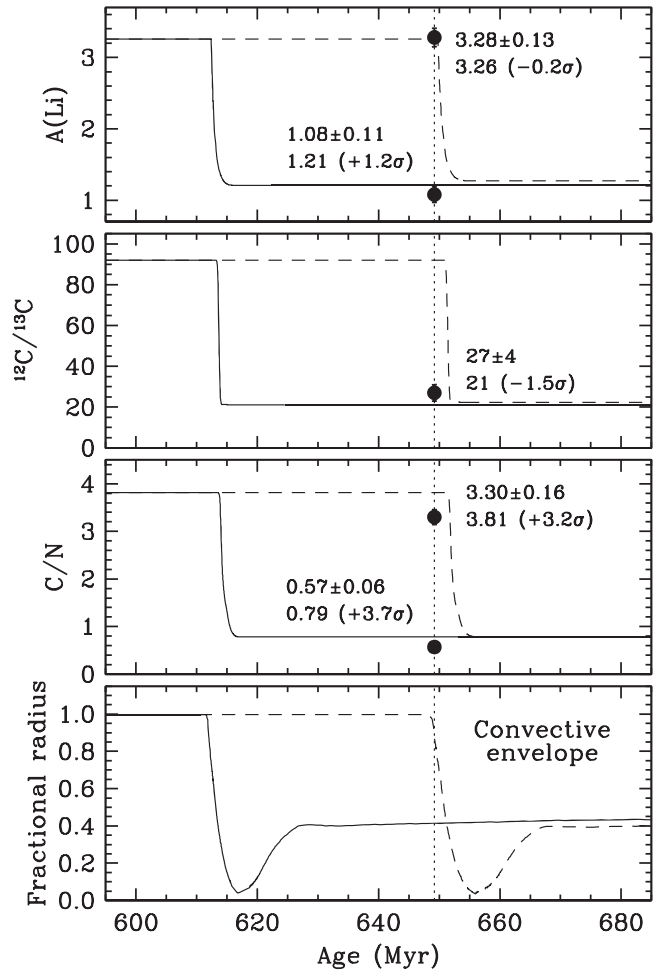

Figure 7. Evolution of chemical diagnostics for Capella occurring near the first dredge-up, as predicted by the models of Claret (2004). Solid lines represent the primary, and dashed lines the secondary. The best-fit age of about 649 Myr is marked by the vertical dotted lines. The lower panel shows the depth of the bottom of the convective zone as a function of time, in units of the stellar radius. The dots represent the measurements, with error bars that are barely visible on this scale. Measured and predicted values are listed near each point, with the deviations listed in parenthesis next to the predictions, in units of the observational errors.

the Granada models for the abundance of lithium, the $^{12}C/^{13}C$ carbon isotope ratio, and the C/N ratio as a function of time. Also shown for reference are the changes in the location of the bottom of the convection zone for each star (lower panel). The measurements of these key chemical diagnostics are represented with dots at the best-fit age of 649 Myr. Generally there is good agreement between theory and observation, except for the C/N ratios that deviate the most.[10] We note, however, that the C/N measurements rely on emission fluxes from spectral lines in the lower transition layers between the stellar chromosphere and the corona (specifically, C IV λ1550.8 and N V λ1238.8; see T09), so they may not strictly represent the abundances in the photosphere (despite some evidence that they do; see, e.g., Böhm-Vitense & Mena-Werth 1992). The convection zone in the secondary star is seen to have just begun deepening, and should reach maximum depth approximately 7 Myr from now, according to these models.

[10] The predicted *difference* between the ratios, however, is in better agreement with the measured difference (to within 1.7σ).

A final test was performed against stellar evolution tracks computed using the Modules for Experiments in Stellar Astrophysics (MESA, revision 7385; see Paxton et al. 2011, 2013).[11] These models use the scaled solar abundances of Asplund et al. (2009), according to which $Z_\odot = 0.0134$. The measured composition of Capella corresponds to a metal mass fraction of about $Z = 0.012$, and the helium abundance follows from an adopted $\Delta Y/\Delta Z = 1.67$, and is $Y = 0.270$. Mass loss is again computed according to the Reimers (1975) prescription, in this case with an efficiency parameter (multiplicative scale factor) of $\eta_R = 0.2$. For this paper we used the "grey_and_kap" surface boundary condition (Paxton et al. 2013), with opacities and equation of state as discussed extensively by Paxton et al. (2011, 2013).

Overshoot mixing across convective boundaries is treated slightly differently than in the models considered previously. MESA uses the exponential decay formalism of Herwig et al. (1997), in which the product of the free parameter f_{ov} and the local pressure scale height provide the scale length over which the diffusion coefficient decays from its value in the convective region. Although MESA allows for the free parameter to take on different values depending on the nuclear burning present in each convective zone, we have opted to use the same f_{ov} value for H- and He-burning regions. For reference, with the choices listed above, we obtained a solar-calibrated mixing length parameter $\alpha_{MLT} = 1.84$, and Herwig et al. (1997) suggest a value of $f_{ov} \simeq 0.02$ for overshoot mixing above the H-burning core.

A grid of MESA evolutionary tracks with the specified composition was computed for each star over broad ranges in α_{MLT} (1.70–2.00, in steps of 0.05) and f_{ov} (0.00–0.04, in steps of 0.01). The models were evolved from the fully convective pre-main sequence to the end of core He burning. Due to the inclusion of mass loss, we increased the initial masses of the stars, as we did before for the Granada models, by $0.0048\,M_\odot$ and $0.0027\,M_\odot$ in this case such that the tracks reach the measured masses at their respective present locations in the H–R diagram. An excellent fit to the properties of both components was achieved at a common age of 588.5 Myr, with all residuals being smaller than 1.2σ. The optimal convective parameters were found to be $\alpha_{MLT} = 1.85$ for the primary and $\alpha_{MLT} = 1.80$ for the secondary, with $f_{ov} = 0.02$ for both stars. The matches in the L–T_{eff} and R–T_{eff} diagrams are illustrated in Figures 8 and 9. Once again the models place the primary at the end of the core helium-burning phase. The age is somewhat younger than obtained from the Granada models (a ∼10% difference), while the age found earlier from the PARSEC models is intermediate between these two. These age differences correlate strongly and have to do mostly with the Z value used in the calculations for each model. The differences in Z at a fixed (measured) [Fe/H] value are in turn a consequence of the different heavy-element mixtures adopted for the Sun in each case.

The predictions from the MESA models regarding the evolution of the surface chemistry of the stars are similar to those from the Granada models. In particular, the predicted $^{12}C/^{13}C$ ratio for the primary at the age of 588.5 Myr is 20.7, and the expected C/N ratios for the primary and secondary are 0.77 and 3.98, respectively, both being somewhat higher than measured.

[11] http://mesa.sourceforge.net/

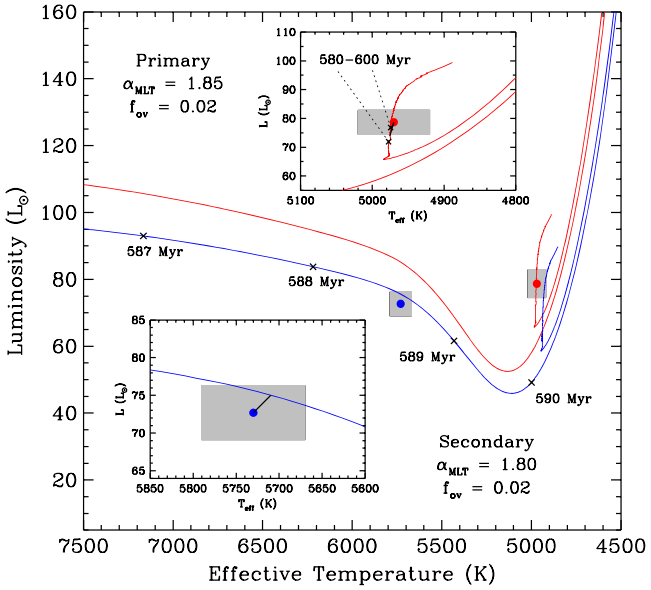

Figure 8. Similar to Figure 5 for the MESA models. The measured metallicity corresponds to $Z = 0.0120$ in these models.

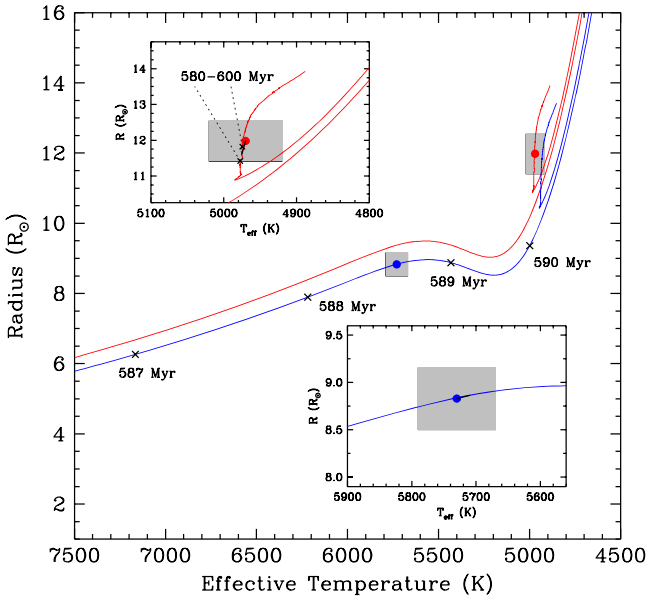

Figure 9. Similar to Figure 8 for the R–$T_{\rm eff}$ plane.

7. TIDAL EVOLUTION

The considerable amount of information available for Capella offers a valuable opportunity to test our understanding of tidal theory in binary stars, in ways those models have not often been challenged before. Such calculations are capable of making detailed predictions about the evolution of the size and shape of the orbit, as well as the rotational properties of the individual components including their spin rate, $\Omega_{\rm rot} = 2\pi/P_{\rm rot}$, and the spin–orbit angle ϕ (angle between the spin axis and the total angular momentum vector of the orbit, sometimes referred to as "obliquity"). In addition to the known orbital elements of Capella, estimates are available also of the rotation periods of both stars, $P_{\rm rot}$ (see Table 3, and T09), and of their projected rotational velocities, $v \sin i$. Our earlier study of the binary examined its tidal evolution considering the turbulent dissipation and radiative damping mechanisms by Zahn et al. (1992), and references therein), as well as the hydrodynamical mechanism of Tassoul & Tassoul (1997), and references therein). These theoretical formulations involve a number of assumptions and simplifications discussed by Zahn (1977) and Hut (1981). In particular, the equations are linearized around the equilibrium state, and are strictly valid only for relatively small eccentricities and near-synchronous rotation, as well as relatively small obliquities.

In this work we have chosen to use the more general equations of tidal evolution by Hut (1981), which are valid for arbitrary eccentricities and rotation rates, although they are still restricted to relatively low mutual inclination angles ϕ. We used a fourth-order Runge–Kutta algorithm to integrate the six coupled differential equations describing the time-dependent changes in the orbital semimajor axis (da/dt), eccentricity (de/dt), angular rotational velocities of both stars ($d\Omega_{\rm rot,A}/dt$, $d\Omega_{\rm rot,B}/dt$), and their spin–orbit angles ($d\phi_{\rm A}/dt$, $d\phi_{\rm B}/dt$). In what follows we normalize the rotation rates to the mean orbital rate $\Omega_{\rm orb}$, for convenience. The relevant stellar properties that also evolve with time, such as the radius, were taken at each integration step directly from the best-fit evolutionary tracks of Claret (2004) discussed in the previous section. The turbulent dissipation timescale for the stellar phases with convective envelopes (later stages for Capella) was adopted from Zahn (1977), whereas the timescale for earlier phases with radiative envelopes follows Claret & Cunha (1997). The initial conditions, which are unknown, were set by trial and error to match the measured values of the orbital period, the eccentricity, and the spin rates at the current age as closely as possible.

The outcome of these calculations is illustrated in the top four panels of Figure 10. Setting the initial values to $P_0 = 220$ days, $e_0 = 0.70$, $(\Omega_{\rm rot,A}/\Omega_{\rm orb})_0 = 320$, and $(\Omega_{\rm rot,B}/\Omega_{\rm orb})_0 = 260$ leads to evolved properties that are very close to those observed at the present age. In particular, the observed super-synchronous rotation rate of the secondary ($\Omega_{\rm rot,B}/\Omega_{\rm orb} = P_{\rm orb}/P_{\rm rot,B} \approx 12$) is well reproduced. Qualitatively the largest difference is perhaps in the orbital eccentricity, which theory predicts should strictly have fallen to zero some 35 Myr ago, driven almost exclusively by the evolution of the primary star. Quantitatively, however, the difference in e between theory and observation is small, as the measured value (if real) is only $e = 0.00089 \pm 0.00011$. While the agreement reached in these four observed properties is not entirely unexpected because we have allowed for four free parameters (the initial values), we note that the good fit was only possible by increasing the nominal efficiency of the tidal dissipation by more than an order of magnitude. Without this increase, we find that the predicted rotational velocities of the stars near the zero-age main-sequence are unreasonably low ($v \sin i \sim 20$ km s^{-1}) for early A-type stars, such as the Capella components would have been. In order to yield more reasonable projected rotational velocities in excess of 100 km s^{-1} we had to increase the efficiency of the tidal mechanisms by a factor of ~40. A similar shortcoming in the efficiency of theory was found earlier
by Claret & Cunha (1997), in their analysis of tidal synchronization and circularization of a sample of detached eclipsing binaries.

Figure 10(f) displays the evolution of the spin–orbit angles for the two stars near the present age, where the integrations have been performed with arbitrary initial values of $\phi_0 = 0.4$ radians (about 23°) for both stars, as we have no direct handle

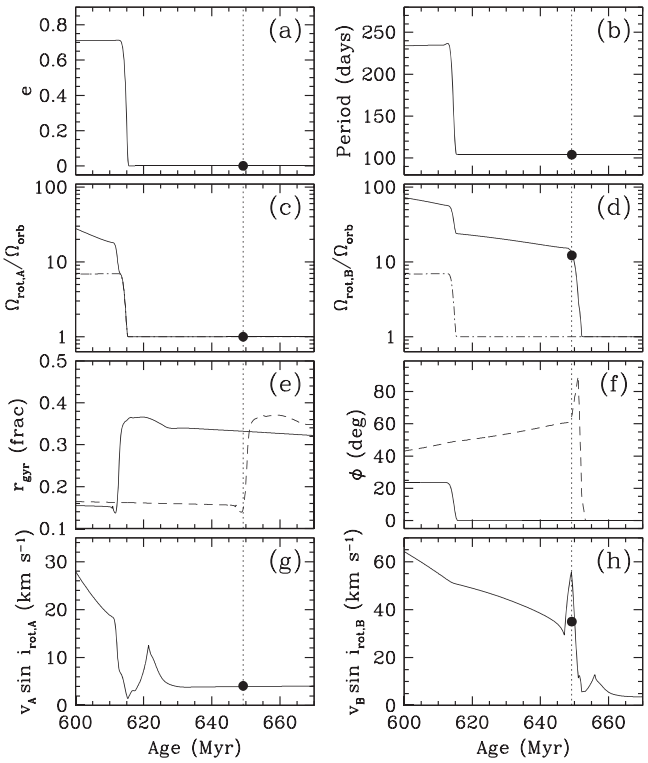

Figure 10. Predicted tidal evolution for Capella according to Hut (1981), compared with the observations (filled circles; error bars are smaller than the point size). (a) Eccentricity evolution. The vertical dotted line in this and the other panels marks the current age of the binary (649 Myr) according to the models by Claret (2004) described in the text. (b) Evolution of the orbital period. (c) and (d) evolution of the spin rate of the primary and secondary, normalized for convenience in terms of the orbital angular velocity. The dot–dashed line represents the evolution of the pseudo-synchronous rotation rate, computed following Equation (42) of Hut (1981). (e) Evolution of the fractional gyration radius of each star, for reference (solid line for primary, dashed for secondary). (f) Evolution of the spin-orbit inclination angle for each star (lines as in previous panel). (g) and (h) predicted projected rotational velocities of the two stars.

on those angles. Tests with other (non-zero) values show that the behavior is qualitatively always the same: the primary's spin axis aligns itself with the orbital axis (i.e., ϕ reaches zero) well before the current age, whereas the secondary remains formally misaligned. The alignment of the primary happens at very nearly the same time that its rotation becomes synchronous and that the orbit circularizes. The spin–orbit angle of the secondary quickly shrinks to zero shortly after the present age (4–5 Myr later), at which time it also synchronizes its rotation with the mean orbital motion. In both cases the changes are the result of significant structural adjustments in the stars, such as a sharp increase in the radius of gyration, $r_{\rm gyr}$, related to the moment of inertia through $I = M\,(r_{\rm gyr}R)^2$ (see Figure 10(e)).

While we cannot measure the present-day values of ϕ, it is possible to gain indirect knowledge about these angles using our spectroscopic estimates of $v \sin i$ along with the measurements of $P_{\rm rot}$ and the radii of both stars. These quantities are trivially related by

$$v \sin i = \frac{2\pi R}{P_{\rm rot}} \sin i_{\rm rot}, \qquad (1)$$

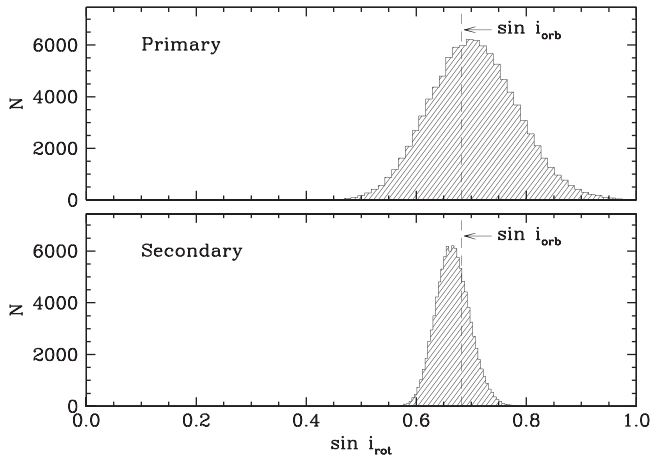

Figure 11. Histograms represent the empirical distributions of sin $i_{\rm rot}$ derived from the measurement of $v \sin i$, $P_{\rm rot}$, and the radius of each star as given in Table 3. The dashed lines mark the value of sin $i_{\rm orb}$ determined from our orbital fit. The good agreement strongly suggests that the spin axes of both stars may in fact be parallel to the orbital axis.

where the inclination angle on the left-hand side (inaccessible to direct observation) is strictly that of the stellar spin axis relative to the line of sight ($i_{\rm rot}$), and also appears on the right. We may thus solve for the sin $i_{\rm rot}$ term on the right-hand side. Figure 11 displays the distributions of sin $i_{\rm rot}$ derived from the propagation of all observational errors in a Monte Carlo fashion. For reference we also show the sine of the orbital inclination angle relative to the line of sight ($i_{\rm orb}$), which is directly measurable from the astrometric observations (Table 3). The close agreement between sin $i_{\rm rot}$ and sin $i_{\rm orb}$ for both stars is highly suggestive that the spin axes may actually be parallel to the orbital axis in space, and this in turn would imply $\phi = 0$. We cannot rule out a difference in quadrants such that the spin axes are tilted with respect to the axis of the orbit while still maintaining the same sine value (e.g., $i_{\rm rot} = 180^\circ - i_{\rm orb}$), but such a coincidence for both stars seems rather unlikely.[12] This indirect empirical evidence that the obliquity may currently be zero for both stars (which would hardly happen by chance) appears to point to a discrepancy with the prediction from tidal theory for the secondary component (Figure 10(f)), whereas for the primary there is good agreement.

It is possible that part of the reason for this difference lies in the small-angle approximation implicit in the tidal differential equations of Hut (1981) for the angle ϕ. However, we note also that the secondary of Capella happens to be in such a rapid state of evolution that theoretical predictions for the spin–orbit angle are extremely sensitive to other details, including those related to structural changes in the stars happening at this stage. Those changes may actually have a larger impact than the dissipation processes themselves (though the latter must also matter). In particular, changes in both the spin rate and the spin–orbit angle are strongly driven in part by the sudden change in the moment of inertia (or equivalently, the gyration radius) illustrated in Figure 10(e). An additional complication is the

[12] Barring this type of situation, conversion of the distributions in Figure 11 to inclination angles yields $i_{\rm rot,A} = 135.^\circ3^{+6.1}_{-6.8}$ and $i_{\rm rot,B} = 138.^\circ2^{+2.3}_{-2.4}$, compared to the orbital value of $i_{\rm orb} = 137.^\circ156 \pm 0.046$.

large ad hoc increase in the efficiency of the tidal mechanism that was required to match other observations, as mentioned earlier. Thus, a definitive assessment of the accuracy of tidal theory related to its other approximations is difficult in this case.

An alternate way of comparing observations with the predictions from tidal and evolution models combined is by examining the evolution of $v \sin i$, which is a spectroscopically measured quantity. It is a function of the stellar radius, the spin rate, and the inclination angle of the rotation axis to the line of sight, $i_{\rm rot}$ (Equation (1)). The latter angle is not directly predicted by theory, but is related to other angles by

$$\cos\phi = \cos i_{\rm orb}\cos i_{\rm rot} + \sin i_{\rm orb}\sin i_{\rm rot}\cos\lambda, \qquad (2)$$

in which the obliquity ϕ can be predicted, $i_{\rm orb}$ is known, and λ is the angle between the sky projections of the spin axis and the orbital axis ("projected obliquity"). The angle λ changes with time and is directly measurable in eclipsing systems by observing the Rossiter–McLaughlin effect. As Capella does not eclipse we have no knowledge of this angle in this case, except for the weak condition that it represents a lower limit to the three-dimensional angle ϕ (see, e.g., Fabrycky & Winn 2009). Equation (2) may be solved for the quantity $\sin i_{\rm rot}$ that we need in order to compute $v \sin i$ with Equation (1), resulting in the quadratic equation

$$A \sin^2 i_{\rm rot} + B \sin i_{\rm rot} + C = 0$$

where

$$A = \cos^2 i_{\rm orb} + \sin^2 i_{\rm orb}\cos^2\lambda$$
$$B = -2\cos\phi\ \sin i_{\rm orb}\cos\lambda$$
$$C = \cos^2\phi - \cos^2 i_{\rm orb}.$$

For the primary star the prediction that $\phi = 0$ near the current epoch means that λ is also zero. Using this value in the equations above to compute the expected evolution of the projected rotational velocity leads to the trend shown in Figure 10(g), where we refer to $v \sin i$ more properly as $v_{\rm A} \sin i_{\rm rot,A}$. Values at times when $\phi \neq 0$ will be somewhat less accurate because the projected obliquity λ may also be different from zero. The predicted value of 4.0 km s^{-1} at the current age is in excellent agreement with the measurement (4.1 ± 0.4 km s^{-1}). The corresponding evolution of $v_{\rm B} \sin i_{\rm rot,B}$ is seen in Figure 10(h). In this case the predicted value at the current age does not match the measurement, and the discrepancy is in part a reflection of the evolution of ϕ that was discussed above, but also has to do with the very rapid changes in the structure of the star (R, $r_{\rm gyr}$) at the present time. Tests in which we changed λ within reason yielded very similar results, and cannot explain the difference.

Finally, it is of interest to verify that the components of Capella have always been detached, as any significant mass transfer earlier in their lives (e.g., through Roche lobe overflow in the primary) would invalidate our comparison with stellar evolution models, which are designed for normal (unperturbed) stars. The fraction of its Roche lobe filled by the primary component depends on its size and also on the size of the orbit, which changes due to tidal forces (Figure 10(b)). The same Granada evolutionary track used above indicates the star attained a maximum radius at the tip of the giant branch of about 38 $R_\odot$ at an age of 617 Myr (MESA models predict a similar maximum size of 36 $R_\odot$), and the filling factor ($R/R_{\rm Roche}$) at the time was approximately 0.63. This indicates that mass transfer through Roche-lobe overflow has not taken place in Capella.

8. DISCUSSION AND CONCLUDING REMARKS

For the first time current stellar evolution models are shown here to provide a satisfactory fit to the observed global properties of both components of Capella at a single age, for a chemical composition equal to that measured. The comparison confirms the long-held but largely unsubstantiated belief that the primary is a clump star, and more precisely, it suggests Capella A is near the end of its core He-burning phase, as indicated consistently by three different sets of models. The principal factors that have allowed the better match are an improvement in the accuracy of the absolute masses, made possible by the high-quality RV measurements of Weber & Strassmeier (2011), and the first robust determination of the metallicity of Capella derived here. Our detailed chemical analysis of the disentangled spectra of the components yields essentially the same near-solar composition for the two stars, which is rather different from the sub-solar abundance the binary was previously assumed to have in our earlier T09 study. All measured properties (masses, radii, temperatures, and independently derived luminosities) are now simultaneously in agreement with the models to within 0.4–1.4σ, depending on the model. This result strengthens our confidence in evolutionary calculations for evolved stars.

Chemical indicators of evolution that differ greatly between the components, such as the ^{12}C/^{13}C ratio, the lithium abundance, and the C/N ratio, are also broadly in agreement with theoretical predictions, though with somewhat larger differences that may be due to either shortcomings in the mixing prescriptions in the models, or observational errors in these delicate measurements. Rarely has it been possible to perform this type of test involving key chemical diagnostics for a binary with two evolved components having well-determined absolute dimensions (M, R, etc.), such as Capella.

On the other hand, the performance of tidal theory as described by the tidal evolution equations of Hut (1981) is not as good. As was noticed previously by Claret & Cunha (1997), we again find that the efficiency of the tidal mechanisms involved seems to be too low by a factor of ~40, if predictions are to be consistent with the large rotational velocities Capella A and B presumably had earlier in their lives as A-type stars ($v \sin i > 100$ km s^{-1}), and at the same time the much lower velocities they now have as evolved stars. Application of an ad hoc adjustment of this magnitude brings agreement, although theory still forecasts a significant misalignment between the spin axis of the secondary and the orbital axis at the present age, whereas empirical evidence based on the direct measurement of the star's radius, rotation period, and $v \sin i$ seems to favor an obliquity consistent with zero. Model predictions about the synchronous rotation of the primary and its spin–orbit alignment do agree with observational clues, as does the supersynchronous rotation of the secondary. A small additional disagreement in that the orbit seems to be very slightly eccentric even though it is expected to be perfectly circular may or may not be significant, as the difference is small.

Finally, another important consequence of our revised chemical composition for Capella concerns the relationship with the coronal abundances, which have been measured by many authors as summarized by T09. Coronal abundances in the Sun are known to depend on the first ionization potential (FIP), in such a way that low-FIP elements (less than 10 eV) are overabundant compared to those with higher FIP (see, e.g., Feldman & Widing 2002). T09 showed this to be the case for Capella as well. Other stars display the opposite effect (see, e.g., Brinkman et al. 2001; Laming 2004). What is less clear from evidence in other stars is whether the low-FIP elements are enhanced relative to the photospheric abundance, or whether it is the high-FIP elements that are depleted compared to the photosphere. T09 adopted a sub-solar photospheric composition for Capella of [m/H] $= -0.34 \pm 0.07$, based on the work of McWilliam (1990), and since this agreed with the measured coronal abundances of the high-FIP elements (see their Figure 18), they concluded it was the low-FIP elements that were enhanced. Interestingly, our revised photospheric abundance of [Fe/H] $= -0.04 \pm 0.06$ leads to precisely the opposite conclusion: now it is the low-FIP elements that agree with the photosphere, and therefore the high-FIP elements are depleted. A recent study by Peretz et al. (2015) of the coronae of stars with super-solar photospheric abundances found the same effect shown by Capella in α Cen A and B, which have somewhat similar temperatures, although these are dwarfs so it is unclear how significant this may be. In any case, Capella now represents a robust point of reference for such studies in evolved and active stars.

We thank Brian Mason (U.S. Naval Observatory) for providing the historical positional measurements of the Capella HL system, and the anonymous referee for helpful comments. The work of G.T. was partially supported by NSF grant AST-1007992, and by Smithsonian Institution Endowment funds. The research has made use of the SIMBAD database, operated at CDS, Strasbourg, France, of NASA's Astrophysics Data System Abstract Service, of the Washington Double Star Catalog maintained at the U.S. Naval Observatory, and of data products from the Two Micron All Sky Survey (2MASS), which is a joint project of the University of Massachusetts and the Infrared Processing and Analysis Center/California Institute of Technology, funded by NASA and the NSF.

APPENDIX
CAPELLA AS A MEMBER OF A MULTIPLE SYSTEM

Over the last two centuries at least half a dozen visual companions to Capella have been recorded at angular separations ranging from 47″ to 12′. Only the widest one, discovered by Furuhjelm (1914), has been shown to be physically associated, and has received the double-star designation Capella H (also ADS 3841 H, GJ 195 A, and LTT 11622, among others). The projected linear separation is ~9500 AU (723″ in position angle 141°). This 10th-magnitude star is of spectral type M1–M2.5, depending on the source, and has the same relatively large proper motion as Capella itself (Furuhjelm 1914; Lepine & Bongiorno 2007) as well as the same parallax (e.g., Daniel & Schlesinger 1920; Adams et al. 1926; Bagnuolo & Hartkopf 1989). The earliest reported RV measurements appear to be those of Abt (1970) at Mount Wilson, of which the first two from consecutive nights in 1921 gave a mean of about +30 km s^{-1}, while a third from 1927 is +48.5 km s^{-1}, with a large probable error. Stauffer & Hartmann (1986) reported a mean RV of +30 ± 1 km s^{-1} based on an unspecified number of CfA spectra using the same setup as T09, and Upgren & Caruso (1988) listed three measurements also from CfA taken in 1986, giving similar values. The first two of these are likely to be based on the same spectra used by Stauffer & Hartmann (1986). Other measurements were reported by Reid et al. (1995) (+31.9 ± 15 km s^{-1}) and Gizis et al. (2002) (+32.7 ± 1.5 km s^{-1}).

Table 4
New Radial Velocity Measurements of Capella H

HJD (2,400,000+)	Julian Year	RV (km s^{-1})	σ_{RV} (km s^{-1})
46475.6230	1986.121	+31.33	0.82
46494.5453	1986.173	+30.97	0.82
46788.8338	1986.978	+31.84	0.70
52986.8030	2003.947	+32.15	0.63
53030.7455	2004.068	+32.19	0.65
53055.6708	2004.136	+32.16	0.55
53078.6029	2004.199	+31.71	0.51
53106.5530	2004.275	+31.43	0.67
53361.7995	2004.974	+31.93	0.58
53419.6511	2005.133	+31.09	0.58
53689.8944	2005.872	+31.08	0.56

In order to supplement these values we report eight additional observations of Capella H with the same instrumentation and procedures described by T09. Radial velocities were derived with the IRAF[13] task `xcsao`, using a synthetic template selected to match the properties of the star with $T_{\rm eff} = 3750$ K and no rotational broadening. The three spectra obtained by Stauffer & Hartmann (1986) and Upgren & Caruso (1988) were reanalyzed in the same way, and our velocities supersede those in the original papers. We list all these measurements in Table 4, on the absolute heliocentric frame defined by the IAU Radial-Velocity Standard Stars (see Stefanik et al. 1999). The 11 velocities show no variation within the measurement errors, and have a mean of +31.63 ± 0.14 km s^{-1}. This is 1.69 ± 0.14 km s^{-1} larger than the center-of-mass velocity of Capella reported in Table 1, and is most likely due to motion in the ~9500 AU orbit.[14]

Capella H was found by Stearns (1936) to have a close (~2″) companion approximately 3.5 mag fainter[15], designated Capella L (also ADS 3841 L and GJ 195 B). Significant changes in position relative to Capella H since the discovery date indicate orbital motion. Thus, the Capella system is a hierarchical quadruple. Historical measurements of the Capella HL binary from the Washington Double Star Catalog were kindly provided by Brian Mason, and are shown in Figure 12. They were obtained mostly with visual micrometers or

[13] IRAF is distributed by the National Optical Astronomy Observatories, which is operated by the Association of Universities for Research in Astronomy, Inc., under contract with the National Science Foundation.

[14] Part of the difference (~0.5 km s^{-1}) is due to the larger gravitational redshift of the M dwarf compared to the pair of giants, and there could also be a contribution from the difference in convective blueshifts. Additionally, there may be a slight offset between the zero-point of the Weber & Strassmeier (2011) velocities and the IAU system.

[15] This visual brightness estimate by Kuiper (1936) may be overestimated, however, since the 2MASS JHK_s magnitudes of the individual components differ by only a few tenths of a magnitude. Alternatively, the companion may itself be multiple.

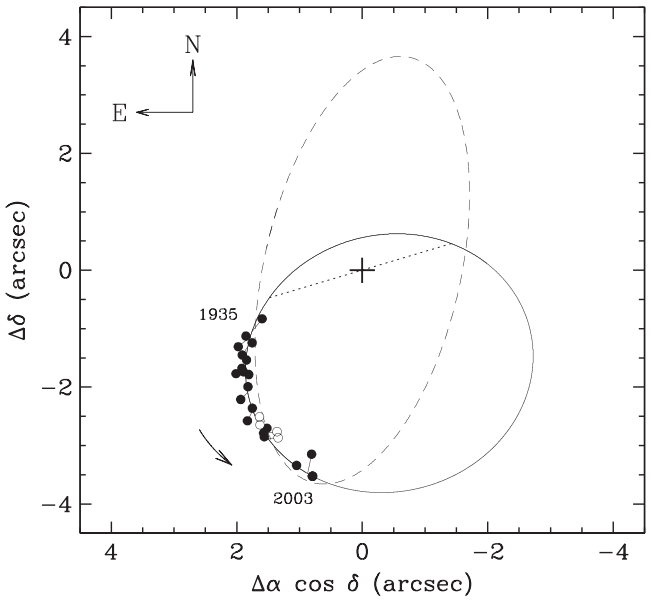

Figure 12. Measurements of the relative position of the Capella HL binary, along with the 388-year orbit by Heintz (1975) (dashed), and our revised orbit (solid). Filled symbols represent measures from the Washington Double Star Catalog, Stearns (1939), and Hełminiak et al. (2009), and open symbols are for the photographic measurements by Heintz. The line of nodes in the revised orbit is indicated with a dotted line, and the motion on the plane of the sky is direct (arrow). The primary (Capella H) is represented by the plus sign. Short line segments connect the measurements with their predicted location on the revised orbit.

photographically. We have supplemented these observations with additional photographic measurements reported by Stearns (1939) and Heintz (1975), as well as more recent and accurate adaptive optics measurements by Hełminiak et al. (2009). A tentative 388-year orbit by Heintz (1975) based on his photographic data and earlier observations is also shown, but does not seem to represent the bulk of the observations very well.

While the astrometric orbit is still largely undetermined because of the short arc covered by the measurements, a helpful constraint may be obtained by making use of rough estimates of the masses of the stars derived from existing near-infrared photometry (2MASS) and the empirical mass–luminosity relation of Delfosse et al. (2000). With inferred values of approximately 0.57 $M_\odot$ and 0.53 $M_\odot$ for Capella H and L, and the use of the orbital parallax from Table 1, Kepler's Third Law then leads to a constraint on the ratio a^3/P^2. A tentative new orbital solution derived in this way, which is also shown in Figure 12, provides a significantly better fit with standard visual elements $P_{\rm orb} \approx 300$ years, $a \approx 3\farcs5$, $e \approx 0.75$, $i \approx 52°$, $\omega_{\rm L} \approx 88°$, $\Omega_{\rm J2000} \approx 288°$, and periastron passage near the year 2220.

REFERENCES

Abt, H. A. 1970, ApJS, 19, 387
Adams, W. S., Joy, A. H., & Humason, M. L. 1926, ApJ, 64, 225
Asplund, M., Grevesse, N., Sauval, A. J., & Scott, P. 2009, ARA&A, 47, 481
Bagnuolo, W. G., Jr., & Hartkopf, W. I. 1989, AJ, 98, 2275
Baranne, A., Queloz, D., Mayor, M., et al. 1996, A&AS, 119, 373
Barlow, D. J., Fekel, F. C., & Scarfe, C. D. 1993, PASP, 105, 476
Batten, A. H., Hill, G., & Lu, W. 1975, PASP, 103, 623
Beavers, W. I., & Eitter, J. J. 1986, ApJS, 62, 147
Böcek Topcu, G., Afşar, M., Schaeuble, M., & Sneden, C. 2015, MNRAS, 446, 3562
Böhm-Vitense, E., & Mena-Werth, J. 1992, ApJ, 390, 253
Bressan, A., Marigo, P., Girardi, L., et al. 2012, MNRAS, 427, 127
Brinkman, A. C., Behar, E., Güdel, M., et al. 2001, A&A, 365, L324
Caffau, E., Ludwig, H.-G., Steffen, M., Freytag, B., & Bonifacio, P. 2011, SoPh, 268, 255
Campbell, W. W. 1901, LicOB, 6, 31
Casagrande, L., Ramírez, I., Meléndez, J., Bessell, M., & Asplund, M. 2010, A&A, 512, 54
Castelli, F., & Kurucz, R. L. 2003, in IAU Symp. 210, Modelling of Stellar Atmospheres, ed. N. Piskunov, W. W. Weiss & D. F. Gray (San Francisco, CA: ASP), A20
Claret, A. 2004, A&A, 424, 919
Claret, A., & Cunha, N. C. S. 1997, A&A, 318, 187
Daniel, Z., & Schlesinger, F. 1920, AJ, 32, 163
Delfosse, X., Forveille, T., Ségransan, D., et al. 2000, A&A, 364, 217
Fabrycky, D. C., & Winn, J. N. 2009, ApJ, 696, 1230
Feldman, U., & Widing, K. G. 2002, PhPl, 9, 629
Flower, P. J. 1996, ApJ, 469, 355
Fuhrmann, K. 2011, ApJ, 742, 42
Furuhjelm, R. 1914, AN, 197, 181
Gizis, J. E., Reid, N. I., & Hawley, S. L. 2002, AJ, 123, 3356
Goos, F. 1908, PhD Dissertation, Friedrich-Wilhelms Univ. Bonn
Grevesse, N. 1984, PhST, T8, 49
Grevesse, N., Noels, A., & Sauval, A. J. 1996, in ASP Conf. Ser. 99, Cosmic Abundances, ed. S. S. Holt & G. Sonneborn (San Francisco, CA: ASP), 117
Grevesse, N., & Sauval, A. J. 1998, SSRv, 85, 161
Hadrava, P. 1995, A&AS, 114, 393
Heintz, W. D. 1975, ApJ, 195, 411
Hełminiak, K. G., Konacki, M., Kulkarni, S. R., & Eisner, J. 2009, MNRAS, 400, 406
Herwig, F., Bloecker, T., Schoenberner, D., & el Eid, M. 1997, A&A, 324, L81
Huby, E., Duchêne, G., Marchis, F., et al. 2013, A&A, 560, A113
Hummel, C. A., Armstrong, J. T., Quirrenbach, Q., et al. 1994, AJ, 107, 1859
Husser, T.-O., Wende-von Berg, S., Dreizler, S., et al. 2013, A&A, 553, AA6
Hut, P. 1981, A&A, 99, 126
Ilijić, S., Hensberge, H., Pavlovski, K., & Freyhammer, L. S. 2004, in ASP Conf. Ser. 318, Spectroscopically and Spatially Resolving the Components of the Close Binary Stars, ed. R. W. Hilditch, H. Hensberge & K. Pavlovski (San Francisco, CA: ASP), 111
Kuiper, G. P. 1936, ApJ, 84, 359
Kulagin, E. S. 1970, SvA, 14, 445
Laming, J. M. 2004, ApJ, 614, 1063
Lehmann, H., Southworth, J., Tkachenko, A., & Pavlovski, K. 2013, A&A, 557, A79
Lepine, S., & Bongiorno, B. 2007, AJ, 133, 889
Lyubimkov, L. S., Lambert, D. L., Kaminsky, B. M., et al. 2012, MNRAS, 427, 11
Lyubimkov, L. S., Lambert, D. L., Korotin, S. A., Rachkovskaya, T. M., & Poklad, D. B. 2015, MNRAS, 446, 3447
Massarotti, A., Latham, D. W., Stefanik, R. P., & Fogel, J. 2008, AJ, 135, 209
McWilliam, A. 1990, ApJS, 74, 1075
Merrill, P. W. 1922, ApJ, 56, 40
Morel, T., Miglio, A., Lagarde, N., et al. 2014, A&A, 564, A119
Newall, H. F. 1900, MNRAS, 60, 418
Pavlovski, K., & Hensberge, H. 2005, A&A, 439, 309
Paxton, B., Bildsten, L., Dotter, A., et al. 2011, ApJS, 192, 3
Paxton, B., Cantiello, M., Arras, P., et al. 2013, ApJS, 208, 4
Peretz, U., Behar, E., & Drake, S. A. 2015, A&A, 577, A93
Ramírez, I., & Meléndez, J. 2005, ApJ, 626, 465
Reddy, A. B. S., Giridhar, S., & Lambert, D. L. 2012, MNRAS, 419, 1350
Reid, I. N., Hawley, S. L., & Gizis, J. E. 1995, AJ, 110, 1838
Reimers, D. 1975, MSRSL, 8, 369
Shcherbakov, A. G., Tuominen, I., Jetsu, L., Katsova, M. M., & Poutanen, M. 1990, A&A, 235, 205
Simon, K. P., & Sturm, E. 1994, A&A, 281, 286
Smalley, B., Smith, K. C., & Dworetsky, M. M. 2001, UCLSYN User Guide, available at http://www.astro.keele.ac.uk/bs/publs/uclsyn.pdf
Stauffer, J. R., & Hartmann, L. W. 1986, ApJS, 61, 531
Stearns, C. L. 1936, AJ, 45, 120
Stearns, C. L. 1939, AJ, 48, 11
Stefanik, R. P., Latham, D. W., & Torres, G. 1999, in ASP Conf. Ser. 185, IAU Coll. 17, Precise Stellar Radial Velocities, ed. J. B. Hearnshaw & C. D. Scarfe (San Francisco, CA: ASP), 354
Strassmeier, K. G., Granzer, T., Weber, M., et al. 2010, AdAst, 2010, 970306
Struve, W. 1939, ZAp, 17, 61
Struve, O., & Kilby, R. F. 1953, ApJ, 117, 272

Tassoul, M., & Tassoul, J.-L. 1997, ApJ, 481, 363
Tomkin, J., Luck, R. E., & Lambert, D. L. 1976, ApJ, 210, 694
Torres, G. 2010, AJ, 140, 1158
Torres, G., Andersen, J., & Giménez, A. 2010, A&ARv, 18, 67
Torres, G., Claret, A., & Young, P. A. 2009, ApJ, 700, 1349
Torres, G., Sandberg Lacy, C. H., Pavlovski, K., et al. 2014, ApJ, 797, 31
Upgren, A. R., & Caruso, J. R. 1988, AJ, 96, 719
Wallerstein, G. 1964, Natur, 204, 367
Wallerstein, G. 1966, ApJ, 143, 823
Weber, M., & Strassmeier, K. G. 2011, A&A, 531, A89
Zahn, J.-P. 1977, A&A, 57, 383
Zahn, J.-P. 1992, in Binaries as Tracers of Stellar Formation, Vol. 253, ed. A. Duquennoy & M. Mayor (Cambridge: Cambridge Univ. Press)
Zucker, S., & Mazeh, T. 1994, ApJ, 420, 806